# Scattering by Cavity-backed Antennas on a Circular Cylinder

Leo C. Kempel and John L. Volakis
Radiation Laboratory
1301 Beal Ave.
Ann Arbor, MI 48109-2122

November 15, 1993

**Abstract**

Conformal arrays are popular antennas for aircraft, spacecraft and land vehicle platforms due to their inherent low weight and drag properties. However, to date there has been a dearth of rigorous analytical or numerical solutions to aid the designer. In fact, it has been common practice to use limited measurements and planar approximations in designing such non-planar antennas. In this paper, we extend the finite element-boundary integral method to scattering by cavity-backed structures in an infinite, metallic cylinder. In particular, we discuss the formulation specifics such as weight functions, dyadic Green's function, implementation details and particular difficulties inherent to cylindrical structures. Special care is taken to ensure that the resulting computer program has low memory demand and minimal computational requirements. Scattering results are presented and validated as much as possible.

# 1 Introduction

Conformal antenna arrays are attractive for aircraft, spacecraft, and land vehicle applications since these antenna systems have low weight, low drag, flexibility, and cost advantages over conventional protruding antennas. The majority of previous studies pertaining to non-planar conformal antennas has been conducted experimentally due to a dearth of rigorous analysis techniques. Traditional rigorous techniques involve an integral equation and are limited in terms of radius of curvature and structural complexity. Some approximate methods have been considered but these are restricted in accuracy and element shape.

Recently, the finite element–boundary integral (FEM-BI) method was successfully employed for the analysis of large cavity-backed planar arrays [1]. The resulting system is sparse due to the local nature of the finite element method, whereas the boundary integral sub-matrix is fully populated. However, by resorting to an iterative solver such as the Biconjugate Gradient (BiCG) method, the boundary integral sub-system may be cast in circulant form allowing use of the Fast Fourier Transform (FFT) in performing the matrix-vector products. This BiCG-FFT solution scheme ensures $\mathcal{O}(N)$ memory demand for the entire FEM-BI system and minimizes the computational requirements.

In this paper, the FEM-BI formulation is extended to scattering by aperture antennas conformal to a cylindrical metallic surface. In contrast to the planar aperture array, the implementation of the cylindrically conformal array requires shell-shaped elements rather than bricks, and the required external Green's function must satisfy the boundary conditions on the surface of the cylinder. In its exact form, this Green's function is an infinite series which imposes unacceptable computational burdens on the method. However, for large radius cylinders, a suitable asymptotic formula is available and herein used for an efficient evaluation of the Green's function. In addition, the resulting BI system is again cast in circulant form to ensure an $\mathcal{O}(N)$ memory demand and to take advantage of the FFT's efficiency when carrying out the matrix-vector product.

A primary difficulty in studying cavity-backed antennas mounted on curved surfaces is the lack of reference data. In this paper, scattering calculations based on the FEM-BI method are compared with data based on different techniques. Although such validation is necessarily limited, it provides con-

fidence in the formulation's accuracy so that this approach may be used in extending the available reference data.

# 2 FEM-BI for Circular Cylinders

In this section, the FEM-BI formulation is developed for cavities recessed in an infinite metallic cylinder, having walls which coincide with constant $\rho$-,$\phi$- or z-surfaces (see figure 1). As usual, the finite element formulation permits substantial modeling flexibility, including cavity inhomogeneities, lumped loads, super/substrate antenna configurations, or microstrip line and so on.

The FEM-BI approach possesses both low memory and computational demand when implemented with a BiCG-FFT solver. Although the system of equations associated with the FEM formulation is sparse, the boundary integral sub-matrix is fully populated. However, if the aperture mesh is a uniform grid, the BiCG-FFT solver may be employed for that portion of the system thus retaining $\mathcal{O}$(N) memory demand for the entire system. In addition, the solver require low computational demand since both sparse matrix-vector products and discrete convolutions using FFTs require only $\mathcal{O}$(NlogN) operations per iteration.

The FEM-BI formulation begins with the weak form of the vector wave equation followed by specification of appropriate vector shape functions and dyadic Green's function. The resulting FEM-BI equations are then used to solve for the total electric fields within the cavity and on the aperture (see for example Volakis *et al.* [2]). For the specific configuration at hand, the weak form of the wave equation can be written as

$$\int_{V_i} \left\{ \frac{\nabla \times \vec{W}_j(\rho,\phi,z) \cdot \nabla \times \vec{W}_i(\rho,\phi,z)}{\mu_r(\rho,\phi,z)} \right.$$
$$\left. -k_o^2 \epsilon_r(\rho,\phi,z) \vec{W}_j(\rho,\phi,z) \cdot \vec{W}_i(\rho,\phi,z) \right\} \rho \, d\rho \, d\phi \, dz$$
$$+(k_o a)^2 \delta_a(j) \delta_a(i) \int_{S_i} \int_{S_j} \left[ \vec{W}_i(a,\phi,z) \cdot \hat{\rho}(a,\phi,z) \times \right.$$
$$\left. \overline{\overline{G}}_2(a,\bar{\phi},\bar{z}) \times \hat{\rho}(a,\phi',z') \cdot \vec{W}_j(a,\phi',z') \right] d\phi' \, dz' \, d\phi \, dz = f_i^{int} + f_i^{ext} \quad (1)$$

In this, $\vec{W}_i$ are vector basis functions with support over the volume $V_i$ which is

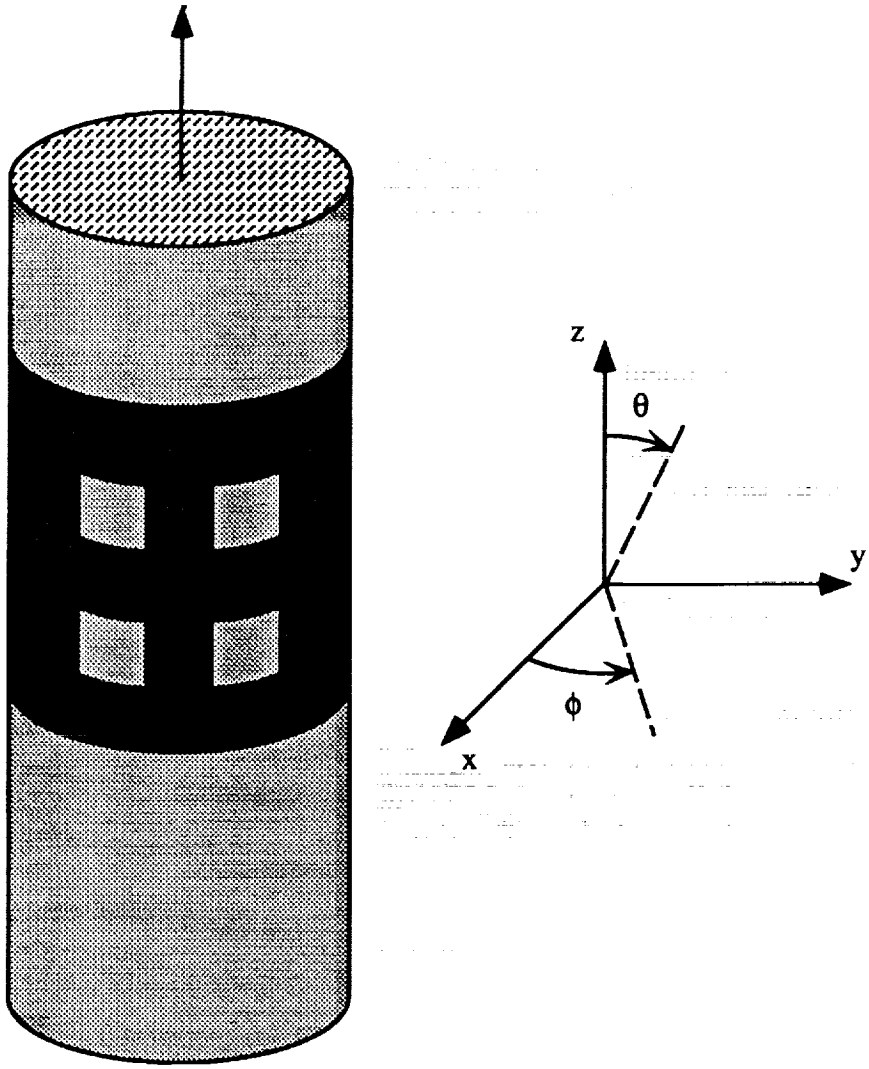


Figure 1: Illustration of a typical cavity-backed antenna situated on a metallic cylinder and the associated coordinate system.

associated with the $i^{th}$ degree of freedom, and in a similar fashion, $S_i$ and $S_j$ represent aperture surfaces associated with the $i^{th}$ and $j^{th}$ degrees of freedom, respectively. The appropriate dyadic Green's function is denoted by $\overline{\overline{G}}_2$ and it has convolutional ($\bar{\phi} = \phi - \phi'$, $\bar{z} = z - z'$) form when evaluated on the surface of the cylinder, $\rho = a$. The unprimed coordinates represent the test point while the primed ones denote the source point. The free-space propagation constant is given by $k_0 = \frac{2\pi}{\lambda_0}$, where $\lambda_0$ is the free-space wavelength. The cavity is filled with an inhomogeneous material having relative constitutive properties $\epsilon_r$ and $\mu_r$. The function $\delta_a(i)\delta_a(j)$ is the product of two Kronecker delta functions. Hence, it identifies which pairs of unknowns belong to the aperture and accordingly contribute to the boundary integral sub-matrix.

The FEM-BI equation (1) may be rewritten in matrix form as

$$\left[\mathcal{A}\right] \begin{Bmatrix} E_j^{ap} \\ E_j^{int} \end{Bmatrix} + \begin{bmatrix} [\mathcal{G}] & [0] \\ [0] & [0] \end{bmatrix} \begin{Bmatrix} E_j^{ap} \\ E_j^{int} \end{Bmatrix} = \begin{matrix} \{f_i^{ext}\} \\ \{0\} \end{matrix} \tag{2}$$

where the entries of $[\mathcal{A}]$ are due to the FEM portion of the formulation and $[\mathcal{G}]$ is the boundary integral sub-matrix. In (2), $E_j^{ap}$ and $E_j^{int}$ denote degrees of freedom associated with the aperture and interior fields, respectively. In this, $f_i^{ext}$ are functions of the external excitation and will be discussed later in the paper.

An important factor in choosing the finite elements for gridding the cavity is the element's suitability for satisfying the mathematical requirements of the formulation as well as the physical features of the antenna system. Traditional node-based finite elements associate the degrees of freedom with the nodal fields and have proven unsatisfactory for three-dimensional electromagnetics applications since they do not correctly represent the null space of the curl operator and hence spurious modes are generated [3, 4]. In contrast, edge-based elements correctly model the curl operator and therefore the electromagnetic fields. In addition, edge-based elements avoid explicit specification of the fields at corners where edge conditions may require a singularity. Jin and Volakis [6] presented edge-based brick elements which are convenient for rectangular-type structures and cavities. For cavities residing in a circular cylinder, shell elements are the natural choice.

Cylindrical shell elements possess both geometrical fidelity and simplicity for cylindrical-rectangular cavities. Figure 2 illustrates a typical shell element which has eight nodes connected by twelve edges: four edges aligned along

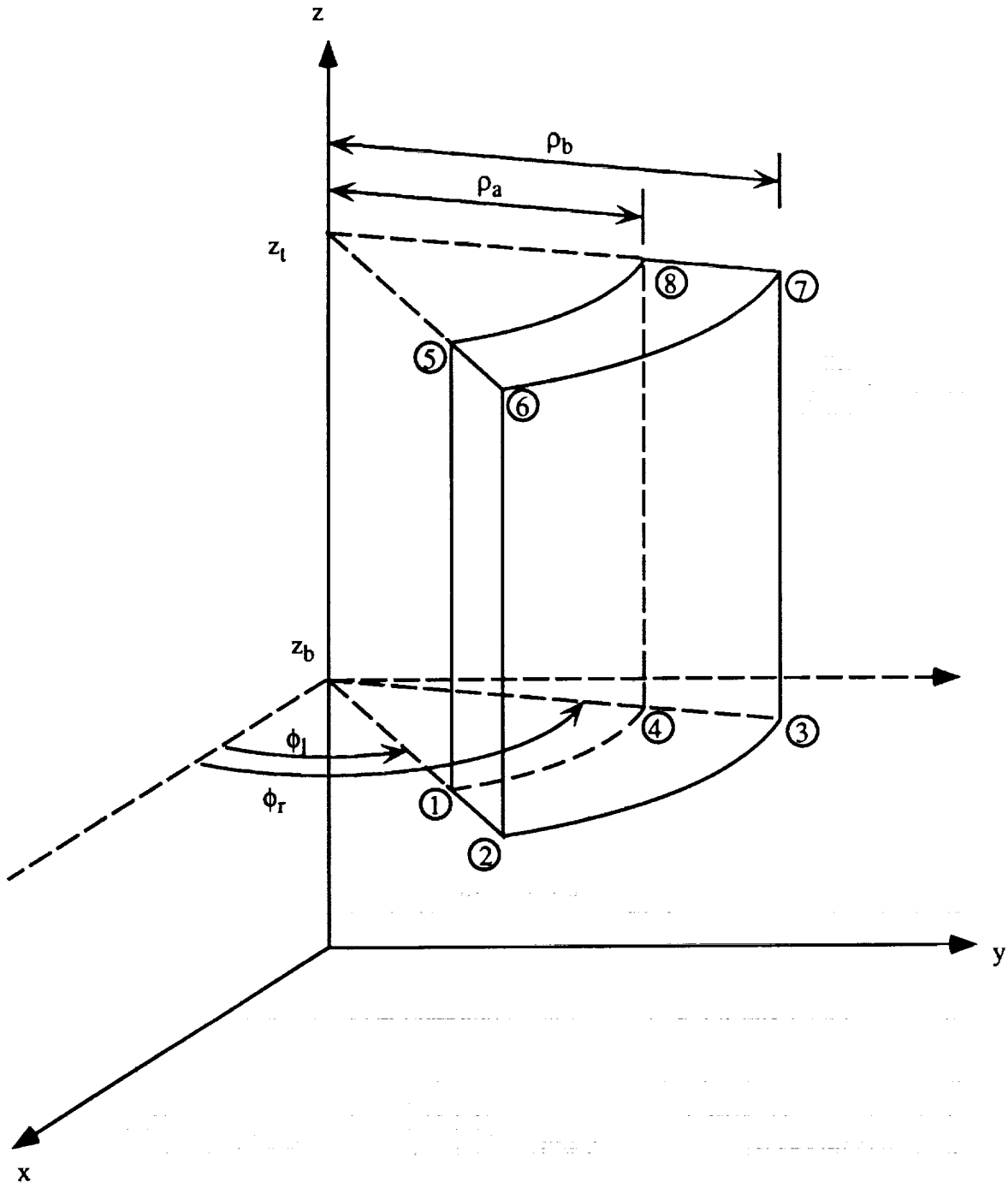


Figure 2: Cylindrical shell element.

each of the three orthogonal directions of the cylindrical coordinate system. Each element is associated with twelve vector shape functions given by

$$\vec{W}_{12}(\rho,\phi,z) = \vec{W}_{\rho}(\rho,\phi,z;\cdot,\phi_r,z_t,+), \quad \vec{W}_{43}(\rho,\phi,z) = \vec{W}_{\rho}(\rho,\phi,z;\cdot,\phi_l,z_t,-)$$
$$\vec{W}_{56}(\rho,\phi,z) = \vec{W}_{\rho}(\rho,\phi,z;\cdot,\phi_r,z_b,-), \quad \vec{W}_{87}(\rho,\phi,z) = \vec{W}_{\rho}(\rho,\phi,z;\cdot,\phi_l,z_b,+)$$

$$\vec{W}_{14}(\rho,\phi,z) = \vec{W}_{\phi}(\rho,\phi,z;\rho_b,\cdot,z_t,+), \quad \vec{W}_{23}(\rho,\phi,z) = \vec{W}_{\phi}(\rho,\phi,z;\rho_a,\cdot,z_t,-)$$
$$\vec{W}_{58}(\rho,\phi,z) = \vec{W}_{\phi}(\rho,\phi,z;\rho_b,\cdot,z_b,-), \quad \vec{W}_{67}(\rho,\phi,z) = \vec{W}_{\phi}(\rho,\phi,z;\rho_a,\cdot,z_b,+)$$

$$\vec{W}_{15}(\rho,\phi,z) = \vec{W}_{z}(\rho,\phi,z;\rho_b,\phi_r,\cdot,+), \quad \vec{W}_{26}(\rho,\phi,z) = \vec{W}_{z}(\rho,\phi,z;\rho_a,\phi_r,\cdot,-)$$
$$\vec{W}_{48}(\rho,\phi,z) = \vec{W}_{z}(\rho,\phi,z;\rho_b,\phi_l,\cdot,-), \quad \vec{W}_{37}(\rho,\phi,z) = \vec{W}_{z}(\rho,\phi,z;\rho_a,\phi_l,\cdot,+) \tag{3}$$

where $\vec{W}_{lk}$ is associated with the edge which is delimited by local nodes (l,k) as shown in figure 2. As seen from (3), three fundamental vector weight functions are required for the complete representation of the shell element. They are

$$\begin{aligned}
\vec{W}_{\rho}(\rho,\phi,z;\tilde{\rho},\tilde{\phi},\tilde{z},\tilde{s}) &= \frac{\tilde{s}\rho_b}{\alpha h}\frac{(\phi-\tilde{\phi})(z-\tilde{z})}{\rho}\hat{\rho} \\
\vec{W}_{\phi}(\rho,\phi,z;\tilde{\rho},\tilde{\phi},\tilde{z},\tilde{s}) &= \frac{\tilde{s}}{th}(\rho-\tilde{\rho})(z-\tilde{z})\hat{\phi} \\
\vec{W}_{z}(\rho,\phi,z;\tilde{\rho},\tilde{\phi},\tilde{z},\tilde{s}) &= \frac{\tilde{s}}{t\alpha}(\rho-\tilde{\rho})(\phi-\tilde{\phi})\hat{z}
\end{aligned} \tag{4}$$

where the element parameters $(\rho_a,\rho_b,\phi_l,\phi_r,z_b,z_t)$ are shown in figure 2, $t = \rho_b - \rho_a$, $\alpha = \phi_r - \phi_l$ and $h = z_t - z_b$. The $\frac{1}{\rho}$-term which appears in the definition of the $\hat{\rho}$-directed weight (4) is essential in satisfying the divergence free requirement, i.e. so that $\nabla \cdot \vec{W}_j = 0$[1]. Note that as the radius of the cylinder becomes large, the curvature of these elements decreases, resulting in weight functions which are functionally similar to the bricks presented

[1] $\vec{W}_j(\rho,\phi,z)$ will only satisfy this requirement within the volume of the element. These weighting functions introduce artificial charges on the faces of the element and are not divergenceless at element interfaces. This is allowable since these elements do not guarantee normal field continuity across the element faces.

by Jin and Volakis [6]. Having specified the vector basis functions, we may proceed to develop the matrix entries for the system (2).

The FEM-BI system is composed of two parts: a sparse FEM matrix and a fully populated BI sub-matrix as shown in (2). The FEM matrix entries are represented by

$$A_{ij} = \frac{1}{\mu_r} I_{st}^{(1)ij} - k_o^2 \epsilon_r I_{st}^{(2)ij} \tag{5}$$

where constant material properties have been assumed within each element. The subscripts $(i,j)$ refer to the row and column of the matrix entry and correspond to the test and source edges, respectively. The auxiliary functions

$$\begin{aligned} I_{st}^{(1)ij} &= \int_{V_i} \nabla \times \vec{W}_s(\rho,\phi,z;\tilde{\rho}_j,\tilde{\phi}_j,\tilde{z}_j,\tilde{s}_j) \cdot \\ &\qquad \nabla \times \vec{W}_t(\rho,\phi,z;\tilde{\rho}_i,\tilde{\phi}_i,\tilde{z}_i,\tilde{s}_i)\rho\, d\rho\, d\phi\, dz \\ I_{st}^{(2)ij} &= \int_{V_i} \vec{W}_s(\rho,\phi,z;\tilde{\rho}_j,\tilde{\phi}_j,\tilde{z}_j,\tilde{s}_j) \cdot \vec{W}_t(\rho,\phi,z;\tilde{\rho}_i,\tilde{\phi}_i,\tilde{z}_i,\tilde{s}_i)\rho\, d\rho\, d\phi\, dz \end{aligned} \tag{6}$$

are identically zero unless both test and source edges share at least one element in common, resulting in a highly sparse system. Physically, such a system is a consequence of the locality property inherent in a partial differential equation formulation. In (6), the direction of the source and test edges are represented by $(s,t) \in \{\rho,\phi,z\}$, respectively. Since the edges of the mesh are aligned along three orthogonal directions, only six combinations of $(s,t)$ are required for $I^{(1)}$ and only three such combinations for $I^{(2)}$ and all of these are evaluated in Appendix A. Since (6) is symmetric with respect to source and test edges, the FEM matrix will also be symmetric.

A lumped impedance post may be included in the formulation by adding a term to (1) and equivalently to (5); surface or sub-surface metallization layers may also be modeled. Radially oriented lumped loads are approximated in the FEM-BI formulation by a filamentary load located at $(\phi_L, z_L)$ [2]. Such posts have length $l$, cross-sectional area $s$ and impedance $Z_L$. The contribution to $[\mathcal{A}]$ is given by

$$A_{ij} = jk_o Z_o \frac{l}{sZ_L} \int_V \frac{\delta(\phi-\phi_L)\delta(z-z_L)}{\rho} W_i(\rho,\phi,z) W_j(\rho,\phi,z) \rho d\rho d\phi dz \tag{7}$$

which may be readily evaluated in closed form. In addition, infinitesimally thin metallization layers may be represented by simply fixing *a priori* the

weight coefficients to zero for weights associated with edges which are tangential to the metal. This is a consequence of using a total electric field formulation. The symmetry and sparsity of the FEM system $[\mathcal{A}]$ is maintained after the addition of these loads while the BI system $[\mathcal{G}]$ remains fully populated and symmetric.

The boundary integral provides an exact boundary condition for mesh closure and its construction relies on a cylindrical dyadic Green's function. The entries of the boundary integral sub-matrix are

$$\begin{aligned} G_{ij} &= (k_o a)^2 \int_{S_i}\int_{S_j} W_t(a,\phi,z;\tilde{\rho}_i,\tilde{\phi}_i,\tilde{z}_i,\tilde{s}_i)\cdot \\ &\quad \left[\hat{\rho}(a,\phi,z)\times\overline{\overline{G}}_2(a,\bar{\phi},\bar{z})\times\hat{\rho}(a,\phi',z')\right] \\ &\quad \cdot W_s(a,\phi',z';\tilde{\rho}_j,\tilde{\phi}_j,\tilde{z}_j,\tilde{s}_j)d\phi'\,dz'\,d\phi\,dz \end{aligned} \tag{8}$$

where the weight functions are given by (4) and evaluated at the surface $\rho = a$. In (8), the dyadic Green's function ($\overline{\overline{G}}_2$) satisfies both the radiation condition and the Neumann boundary condition at $\rho = a$. This dyadic Green's function may be expressed exactly [8]

$$\begin{aligned} G^{zz}(a,\bar{\phi},\bar{z}) &= -\frac{1}{(2\pi)^2}\sum_{n=-\infty}^{\infty}\int_{-\infty}^{\infty}\left(\frac{k_\rho}{k_o}\right)^2\frac{1}{\gamma}\frac{H_n^{(2)}(\gamma)}{H_n'^{(2)}(\gamma)}e^{j(n\bar{\phi}-k_z\bar{z})}dk_z \\ G^{\phi z}(a,\bar{\phi},\bar{z}) &= -\frac{1}{(2\pi)^2}\sum_{n=-\infty}^{\infty}\int_{-\infty}^{\infty}\left(\frac{nk_z}{k_o^2 a\gamma}\right)\frac{H_n^{(2)}(\gamma)}{H_n'^{(2)}(\gamma)}e^{j(n\bar{\phi}-k_z\bar{z})}dk_z \\ G^{\phi\phi}(a,\bar{\phi},\bar{z}) &= \frac{1}{(2\pi)^2}\sum_{n=-\infty}^{\infty}\int_{-\infty}^{\infty}\frac{1}{\gamma}\left[\frac{H_n'^{(2)}(\gamma)}{H_n^{(2)}(\gamma)}-\left(\frac{nk_z}{k_o a k_\rho}\right)^2\frac{H_n^{(2)}(\gamma)}{H_n'^{(2)}(\gamma)}\right]e^{j(n\bar{\phi}-k_z\bar{z})}dk_z \end{aligned} \tag{9}$$

where $\gamma = k_\rho a$ and $k_\rho = \sqrt{k_o^2 - k_z^2}$. However, for large radius cylinders, (9) is computationally prohibitive. In these cases, which are of main concern in this paper, it is advantageous to employ an asymptotic expression for $\overline{\overline{G}}_2$ [9, 10, 11, 12]. These employ a creeping wave series expansion of which only the two direct path contributions (see figure 3) are retained. The formula due to Pathak and Wang [9]

$$G^{zz}(a,\bar{\phi},\bar{z}) \sim -\frac{jk_o}{2\pi}qe^{-jk_o s}\left\{\left(cos^2\theta + q(1-q)(2-3cos^2\theta)\right)v(\beta)\right\}$$

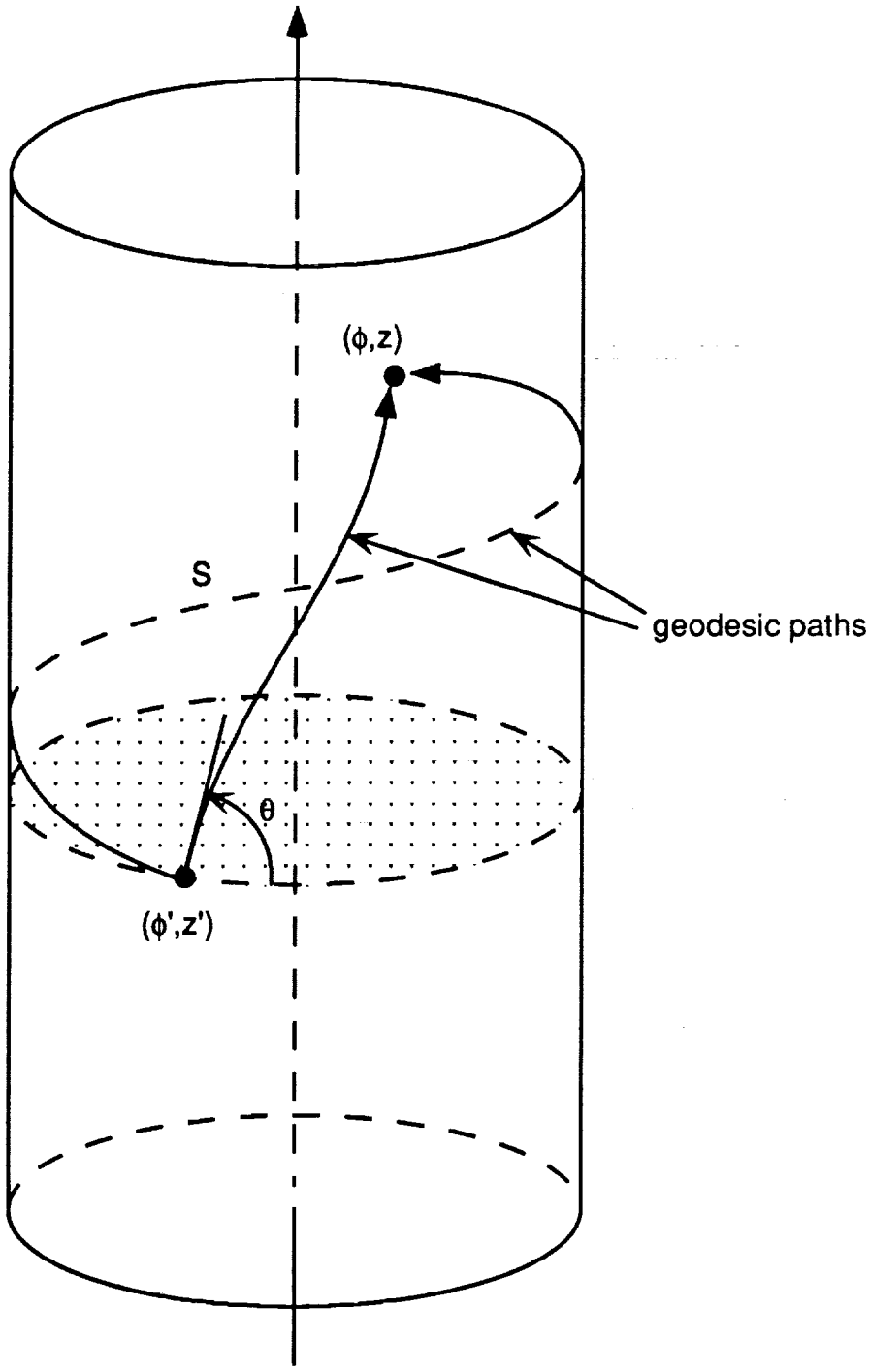


Figure 3: Geodesic paths on a circular cylinder.

$$
\begin{aligned}
G^{\phi z}(a,\bar{\phi},\bar{z}) &\sim \frac{jk_o}{2\pi} q e^{-jk_o s} \sin\theta\cos\theta \Big\{ \left(1 - 3q(1-q)\right) v(\beta) \Big\} \\
G^{\phi\phi}(a,\bar{\phi},\bar{z}) &\sim -\frac{jk_o}{2\pi} q e^{-jk_o s} \Big\{ \left(sin^2\theta + q(1-q)(2-3sin^2\theta)\right) v(\beta) \\
&\quad + q\left[sec^2\theta\left(u(\beta) - v(\beta)\right)\right] \Big\}
\end{aligned}
\tag{10}
$$

where $\beta = ks\left[\frac{cos^2\theta}{\sqrt{2}k_o a}\right]^{\frac{2}{3}}$ and $q = \frac{j}{k_o s}$ has proven quite accurate. In the definition of $\beta$, s is the usual geodesic path length ($s = \sqrt{(a\bar{\Phi})^2 + z^2}$) and $\theta$ is the direction of the trajectory $\left(\theta = tan^{-1}\left[\frac{a\bar{\Phi}}{z}\right]\right)$. Depending on which of the two direct paths (shown in figure 3) is used, $\bar{\Phi} = \bar{\phi}$ or $\bar{\Phi} = 2\pi - \bar{\phi}$. The soft and hard Fock functions, $u(\beta)$ and $v(\beta)$ respectively, are characteristic of on-surface creeping wave interactions and have been extensively investigated by Logan [13]. Although computation of the Green's function (10) is now tractable, evaluation of (8) must be done so that a discrete convolutional system is maintained and the singularity of (8) at $s = 0$ is properly treated.

Care must be taken in evaluating (8) so that the overall storage requirement remains $\mathcal{O}$(N) and the singular integrals of (8) are accurately computed. If uniform zoning is used, the resulting sub-matrix ($[\mathcal{G}]$) is block Toeplitz and hence amenable to solution using the BiCG-FFT method. For the non-selfcell contributions, mid-point integration may be used while a regularization procedure must be employed for the self-cell. Bird [12] noted that (10) recovers the metallic screen Green's function when $\beta = 0$ within the available approximation order. This suggests that (8) may be regularized by adding and subtracting from (10) the function

$$
2\overline{\overline{G}}_o(a,\bar{\phi},\bar{z}) = \left[\overline{\overline{I}} + \frac{\nabla\nabla}{k_o^2}\right]\frac{e^{-jk_o R}}{2\pi R} \quad ; \quad R = |\vec{r} - \vec{r}'| \tag{11}
$$

which is the free-space dyadic Green's function multiplied by two. The resulting regularized Green's function (curvature contribution) is given by

$$
\tilde{G}^{zz}(a,\bar{\phi},\bar{z}) \sim -\frac{jk_o}{2\pi} q e^{-jk_o s}\Big\{ \left(cos^2\theta + q(1-q)(2-3cos^2\theta)\right)\left[v(\beta) - 1\right] \Big\}
$$

$$\begin{aligned}
\tilde{G}^{\phi z}(a,\bar{\phi},\bar{z}) &\sim \frac{jk_o}{2\pi}qe^{-jk_o s}\sin\theta\cos\theta\Big\{\,(1-3q(1-q))\,[v(\beta)-1]\,\Big\} \\
\tilde{G}^{\phi\phi}(a,\bar{\phi},\bar{z}) &\sim -\frac{jk_o}{2\pi}qe^{-jk_o s}\Big\{\,\Big(sin^2\theta+q(1-q)(2-3sin^2\theta)\Big)\,[v(\beta)-1] \\
&\quad +q\left[sec^2\theta\,(u(\beta)-v(\beta))\right]\Big\}
\end{aligned} \tag{12}$$

and since it is no longer singular it may be evaluated numerically. The planar contribution may be calculated in the manner described previously by Jin and Volakis [5]. The FEM-BI matrix has now been fully developed and it remains to specify the excitation function for external sources.

# 3 Plane Wave Excitation

Plane wave excitation of the geometry is considered in this section for scattering analysis. The use of the exact boundary condition in (1) allows coupling of an exterior excitation field into the cavity. We will describe the form of the source functional, $f_i^{ext}$, and discuss its numerical implementation.

The forcing functional, due to exterior sources ($f_i^{ext}$) is given by

$$f_i^{ext} = jZ_o k_o a \int_{S_i} \vec{W}_i(a,\phi',z')\cdot\hat{\rho}(a,\phi',z')\times\vec{H}^{cyl}(a,\phi',z')d\phi'\,dz' \tag{13}$$

where $\vec{W}_i(\rho,\phi,z)$ is the testing weight for the $i^{th}$ row of the matrix and $\vec{H}^{cyl}$ represents the magnetic field on the cylinder's surface in the absence of the cavity. A plane wave

$$\begin{aligned}
\vec{E}^i &= \hat{e}^i e^{-jk_o(\hat{k}^i\cdot\vec{r})} \\
\vec{H}^i &= Y_o(\hat{k}^i\times\hat{e}^i)e^{-jk_o(\hat{k}^i\cdot\vec{r})} \\
&= Y_o\left[\hat{\rho}^i\sin\gamma\cos\theta_i-\hat{\phi}^i\cos\gamma-\hat{z}\sin\gamma\sin\theta_i\right]e^{jk_o[\rho\sin\theta_i\cos(\phi-\phi_i)+z\cos\theta_i]}
\end{aligned} \tag{14}$$

is assumed to be incident on the cylinder from the direction ($\theta_i$,$\phi_i$) where $\gamma$ is the polarization angle and $\hat{e}^i = \hat{\theta}^i\cos\gamma+\hat{\phi}^i\sin\gamma$ is the electric field polarization. The total surface field is given by the sum of the incident

and corresponding scattered field from the infinite metallic cylinder [14]. Specifically,

$$\begin{aligned}\vec{H}^{cyl}(a,\phi,z) &= \vec{H}^{i}(a,\phi,z)+\vec{H}^{s}_{cyl}(a,\phi,z)\\ &= \hat{\phi}H^{cyl}_{\phi}+\hat{z}H^{cyl}_{z}\end{aligned} \tag{15}$$

where

$$\begin{aligned}H^{cyl}_{\phi}(a,\phi,z) &= -2Y_o\frac{e^{jk_o\cos\theta_i z}}{\pi k_o a\sin\theta_i}\sum_{n=-\infty}^{\infty}\left[\frac{\cos\gamma}{H^{(2)}_n(k_oa\sin\theta_i)}+\right.\\ &\qquad \left. j\frac{n}{k_oa\sin\theta_i}\frac{\sin\gamma\cos\theta_i}{H^{'(2)}_n(k_oa\sin\theta_i)}\right]e^{jn(\frac{\pi}{2}+\phi-\phi_i)}\\ H^{cyl}_{z}(a,\phi,z) &= j2Y_o\frac{\sin\gamma}{\pi k_o a}e^{jk_o\cos\theta_i z}\sum_{n=-\infty}^{\infty}\left[\frac{e^{jn(\frac{\pi}{2}+\phi-\phi_i)}}{H^{'(2)}_n(k_oa\sin\theta_i)}\right]\end{aligned} \tag{16}$$

is obtained from traditional modal analysis. These expressions may be approximated by retaining only a few terms of the series if $k_oa\sin\theta_i$ is small. However, as this parameter becomes large (e.g. for large a and $\theta_i \rightarrow 90^o$), (16) may be replaced with equivalent asymptotic representations similar to those considered earlier. Utilizing Watson's transformation and Fock theory [14] in connection with (16), we find that

$$\begin{aligned}H^{cyl}_{z} &\sim -Y_o\sin\gamma\sin\theta_i e^{jk_o\cos\theta_i z}\sum_{p=1}^{2}e^{-jk_oa\sin\theta_i\Phi_p}\left[g^{(0)}(m\Phi_p)\right]^*\\ H^{cyl}_{\phi} &\sim j2Y_o\cos\gamma\frac{m^2}{k_oa\sin\theta_i}e^{jk_o\cos\theta_i z}\sum_{p=1}^{2}e^{-jk_oa\sin\theta_i\Phi_p}\left[f^{(0)}(m\Phi_p)\right]^*\\ &\quad -Y_o\sin\gamma\cos\theta_i e^{jk_o\cos\theta_i z}\sum_{p=1}^{2}(-1)^p e^{-jk_oa\sin\theta_i\Phi_p}\left[g^{(0)}(m\Phi_p)\right.\\ &\qquad \left.-j\frac{m}{k_oa\sin\theta_i}g^{(1)}(m\Phi_p)\right]^*\end{aligned} \tag{17}$$

in which $\Phi_1 = \frac{3\pi}{2}-(\phi-\phi_i)$, $\Phi_2 = (\phi-\phi_i)-\frac{\pi}{2}$, $m = \left[\frac{k_oa\sin\theta_i}{2}\right]^{\frac{1}{3}}$, and complex conjugation is denoted by an asterisk. The appropriate far-zone Fock functions ($g^{(0)}$, $g^{(1)}$ and $f^{(0)}$) are given by Logan [13].

The asymptotic formulas (17) are quite accurate except in the geometrical optics region ($\phi \approx \phi_i$). In this case, Goriainov's [15] expressions

$$
\begin{aligned}
H_z^{cyl} \sim\ & -Y_o \sin\alpha \sin\theta_i e^{jk_o \cos\theta_i z} \Big\{ e^{-jk_o a \sin\theta_i \Phi_1} \left[ g^{(0)}(m\Phi_1) \right]^* \\
& + e^{jk_o a \sin\theta_i \cos(\phi-\phi_i)} \left[ G(-m\cos(\phi-\phi_i)) \right]^* \Big\} \\
H_\phi^{cyl} \sim\ & j2Y_o \cos\alpha \frac{m^2}{k_o a \sin\theta_i} e^{jk_o \cos\theta_i z} \Big\{ e^{-jk_o a \sin\theta_i \Phi_1} \left[ f^{(0)}(m\Phi_1) \right]^* \\
& + e^{jk_o a \sin\theta_i \cos(\phi-\phi_i)} \left[ F(-m\cos(\phi-\phi_i)) \right]^* \Big\} \\
& + Y_o \sin\alpha \cos\theta_i e^{jk_o \cos\theta_i z} \Big\{ e^{-jk_o a \sin\theta_i \Phi_1} \Big[ g^{(0)}(m\Phi_1) \\
& - j \frac{m}{k_o a \sin\theta_i} g^{(1)}(m\Phi_1) \Big]^* \\
& - e^{jk_o a \sin\theta_i \cos(\phi-\phi_i)} \Big[ G(-m\cos(\phi-\phi_i)) \\
& - j \frac{m}{k_o a \sin\theta_i} G^{(1)}(-m\cos(\phi-\phi_i)) \Big]^* \Big\}
\end{aligned}
\tag{18}
$$

have been found to be more accurate and can be used instead of (17). The Fock functions ($G$, $G^{(1)}$ and $F$) are again defined in Logan [13]. These surface field expressions may be used to calculate the entries of the column vector $\{f_i^{ext}\}$ efficiently via a numerical evaluation of (13). In particular, the modal series (16) is used when $k_o a \sin\theta_i \leq 10$ and either (17) or (18) for $k_o a \sin\theta_i > 10$ as appropriate. With the excitation functional and the FEM-BI matrix now specified, the BiCG-FFT method [16, 17] may be used to determine the unknown electric fields within the cavity.

# 4 Scattering

Once the cavity aperture and volume electric fields have been determined by solving (2) for an external excitation, the radar cross section (RCS) may be calculated. The far-zone fields may be computed by integrating the aperture fields with a suitable Green's function. In this section we present the relevant

formula for calculating the far-zone fields and hence the RCS due to excitation by a plane wave (14).

To determine the far-zone fields, we begin with the integral representation for the scattered magnetic field in terms of the aperture fields. We have

$$\begin{aligned}\vec{H}^s(r,\theta,\phi) &= jY_o k_o a \int_S \overline{\overline{G}}_2(r,\theta,\phi;a,\phi',z') \cdot \\ &\quad \left[\hat{\rho}(a,\phi',z') \times \vec{E}(a,\phi',z')\right] d\phi'\, dz' \end{aligned} \tag{19}$$

with (r,$\theta$,$\phi$) indicating the observation point in spherical coordinates. When the observation point is very far from the cylinder, the dyadic Green's function in (19) can be replaced by its far-zone representation

$$\overline{\overline{G}}_2(r,\theta,\phi;a,\phi',z') \sim \frac{e^{-jk_o r}}{k_o r}\left[G^{\theta\phi}\hat{\theta}\hat{\phi}' + G^{\theta z}\hat{\theta}\hat{z} + G^{\phi\phi}\hat{\phi}\hat{\phi}'\right] \tag{20}$$

where the unprimed unit vectors are functions of the observation position and the primed ones are functions of the integration point in (19). The components of this far-zone Green's function

$$\begin{aligned} G^{\theta\phi} &\sim \frac{j}{(2\pi)^2}\frac{2k_o\cos\theta}{(k_o a\sin\theta)^2}e^{jk_o\cos\theta z'}\sum_{n=-\infty}^{\infty}\frac{n}{H_n'^{(2)}(k_o a\sin\theta)}e^{jn(\frac{\pi}{2}+(\phi-\phi'))} \\ G^{\theta z} &\sim \frac{j}{(2\pi)^2}\frac{2}{a}e^{jk_o\cos\theta z'}\sum_{n=-\infty}^{\infty}\frac{1}{H_n'^{(2)}(k_o a\sin\theta)}e^{jn(\frac{\pi}{2}+(\phi-\phi'))} \\ G^{\phi\phi} &\sim \frac{j}{(2\pi)^2}\frac{2}{a\sin\theta}e^{jk_o\cos\theta z'}\sum_{n=-\infty}^{\infty}\frac{1}{H_n^{(2)}(k_o a\sin\theta)}e^{jn(\frac{\pi}{2}+(\phi-\phi'))} \end{aligned} \tag{21}$$

are determined by a mode matching procedure. As one might expect, these series converge rather slowly for large $k_o a\sin\theta$. They must therefore be recast in another form by employing Watson's transformation and Fock theory as was done previously (17). In doing so, we obtain

$$\begin{aligned} G^{\theta\phi} &\sim \frac{k_o\cos\theta}{4\pi}e^{jk_o\cos\theta z'}\sum_{p=1}^{2}(-1)^p e^{-jk_o a\sin\theta\Phi_p}\left[g^{(0)}(m\Phi_p) - j\frac{m}{k_o a\sin\theta}g^{(1)}(m\Phi_p)\right]^* \\ G^{\theta z} &\sim -\frac{k_o\sin\theta}{4\pi}e^{jk_o\cos\theta z'}\sum_{p=1}^{2}e^{-jk_o a\sin\theta\Phi_p}\left[g^{(0)}(m\Phi_p)\right]^* \\ G^{\phi\phi} &\sim \frac{m^2}{2a\pi\sin\theta}e^{jk_o\cos\theta z'}\sum_{p=1}^{2}e^{-jk_o a\sin\theta\Phi_p}\left[f^{(0)}(m\Phi_p)\right]^* \end{aligned} \tag{22}$$

where the Fock functions are the same as those used with (17) due to reciprocity. As was the case for the plane wave source, Goriainov's [15] approximations are more accurate in the geometrical optics region ($\phi' \approx \phi$) and similar expressions may be obtained for (22) as was found for (17). The far-zone scattered field can be computed numerically by using (19) and either the series or asymptotic formula as appropriate. Having done so, the RCS is calculated from

$$\sigma(\theta,\phi) = \lim_{r\to\infty} 4\pi r^2 \frac{|\vec{H}^s(r,\theta,\phi)|}{|\vec{H}^i(r,\theta,\phi)|} \tag{23}$$

Above we presented a FEM-BI formulation suitable for modeling cavity-backed structures embedded in a circular cylinder. Next, we consider a few numerical calculations aimed at validating this formulation and in giving us an appreciation on how the cylinder's curvature influences the scattering parameters.

# 5 Results

Having solved for the electric fields induced by an incident plane wave, the resulting RCS data must be validated with known results. As previously mentioned, available measured or computed data is rather scarce and as a consequence, we are forced to rely on limiting cases in order to validate this work. As the radius of curvature decreases, a cylindrical-rectangular cavity will approximate a planar-rectangular cavity. Another limiting case involves comparison of an elongated 3-D cavity with a corresponding 2-D cavity for normal incidence ($\theta_i = 90^o$). Finally, we may compare our infinite cylinder results with a finite Body of Revolution (BOR) model for certain polarizations and angles of incidence. We begin with the quasi-planar case.

The first validation effort for scattering by cavity-backed patch antennas relies on the fact that a small patch on a very large radius cylinder is quasi-planar and approximates rather well an equal sized planar patch. For our test we chose as a reference a planar $1.448'' \times 1.083''$ patch residing on a $2.89'' \times 2.10'' \times 0.057''$ cavity filled with a dielectric having $\epsilon_r = 4$. The equivalent patch on a $10\lambda$ cylinder is $6.46^o \times 1.083''$ residing on a $12.90^o \times 2.10'' \times 0.057''$ cavity. Figure 4 shows the results for the patch on a large radius cylinder with corresponding data for the planar cavity-backed patch. Clearly, the two

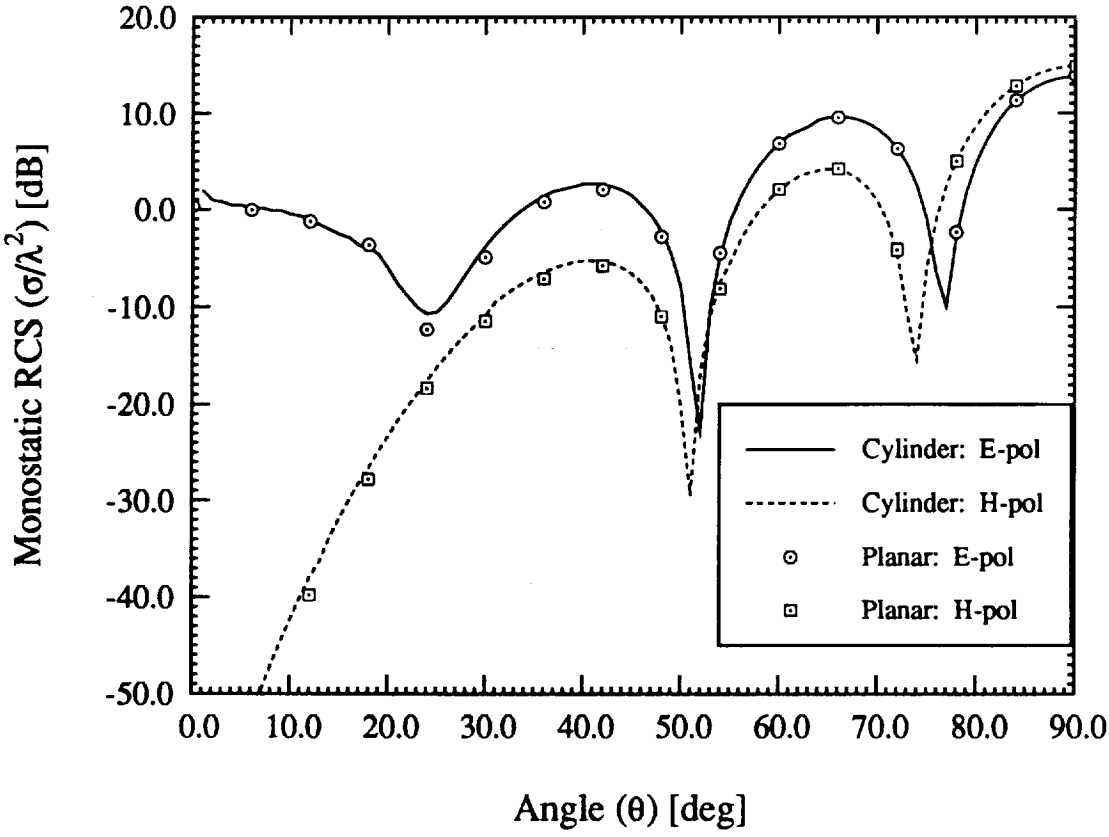


Figure 4: Comparison of RCS for a planar patch ($1.488'' \times 1.083''$) residing on a $2.89'' \times 2.10'' \times 0.059''$ cavity filled with $\epsilon_r = 4$ dielectric and a corresponding quasi-planar patch on a large radius ($10\lambda_0$) cylinder.

RCS patterns are in excellent agreement, and although figure 4 illustrates only monostatic scattering in the $\phi = 0^o$ plane, additional runs for normally incident monostatic scattering and various bistatic situations yield similar agreement.

Comparisons may also be made for elongated cavities and 2-D MoM results. Long narrow cavities have very little axial interaction for principal plane ($\theta = 90^o$) excitation and therefore results based on this formulation should compare well with corresponding 2-D data. It is well known that the RCS of the 3-D scattering body of length $L \gg \lambda_0$ is related to the corresponding 2-D scattering of the same cross section via the relation

$$\sigma_{3D} = 2\left(\frac{L}{\lambda_0}\right)^2 \sigma_{2D} \tag{24}$$

Such a comparison is shown in figure 5 for monostatic scattering by a $45^o \times 5\lambda \times 0.1\lambda$ cavity for both principal polarizations. Once again the agreement between the two results is excellent, thus providing a partial validation of the formulation for highly curved geometries. We remark that similar agreement has been observed for bistatic scattering in the $\theta = 90^o$ plane.

The planar approximation eliminates the effects of curvature, which is a primary interest in this work, and the 2-D comparisons done above are only valid for normal incidence. To consider oblique incidence on a highly curved structure, we resort to comparisons with a Body of Revolution (BOR) code for wraparound cavities. Since the BOR code can only model finite structures, we simulate an infinite cylinder by coherently subtracting the far-zone fields of the finite structure without a cavity from similar data which includes the cavity. Such an procedure mimics common measurement practices and was found suitable for near normal incidence and quite acceptable near grazing incidence in the case of H-polarization ($\alpha = 90^o$). An example calculation for the latter case is given in figure 6 where a bistatic scattering pattern is presented in the $\phi = 0^o$ plane due to a plane wave incident at ($\theta_i = 90^o$,$\phi_i = 0^o$). Clearly, there is good agreement between the FEM-BI results and data based on the BOR formulation.

The previous comparisons serve to validate the formulation. Having done so, it is instructive to examine the effect that curvature has on the scattering properties of cavity-backed patch antennas. Consider a 2 cm $\times$ 3 cm patch residing on a 5.0 cm $\times$ 6.0 cm $\times$ 0.07874 cm cavity which is filled with a dielectric having $\epsilon_r = 2.17$. Figures 7 and 8 illustrate the behavior of

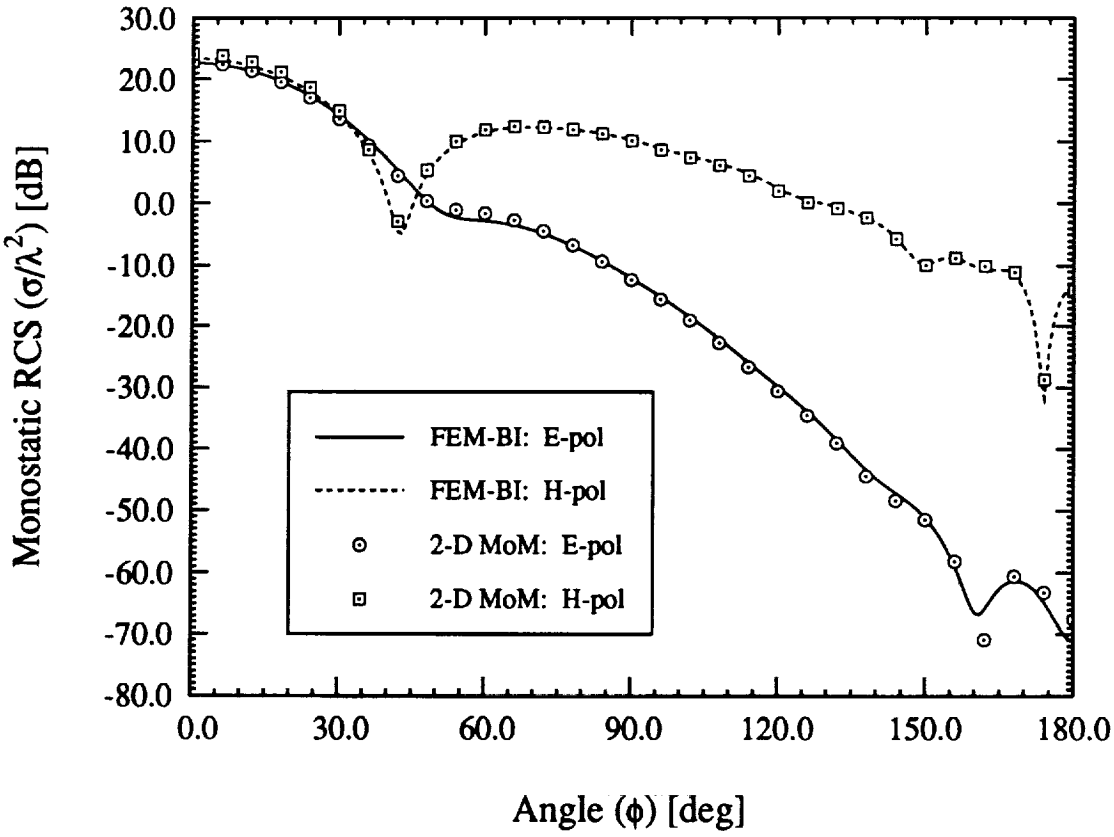


Figure 5: Comparison of 2-D MoM results and FEM-BI RCS results for a $45^o \times 5\lambda_0 \times 0.1\lambda_0$ air-filled cavity.

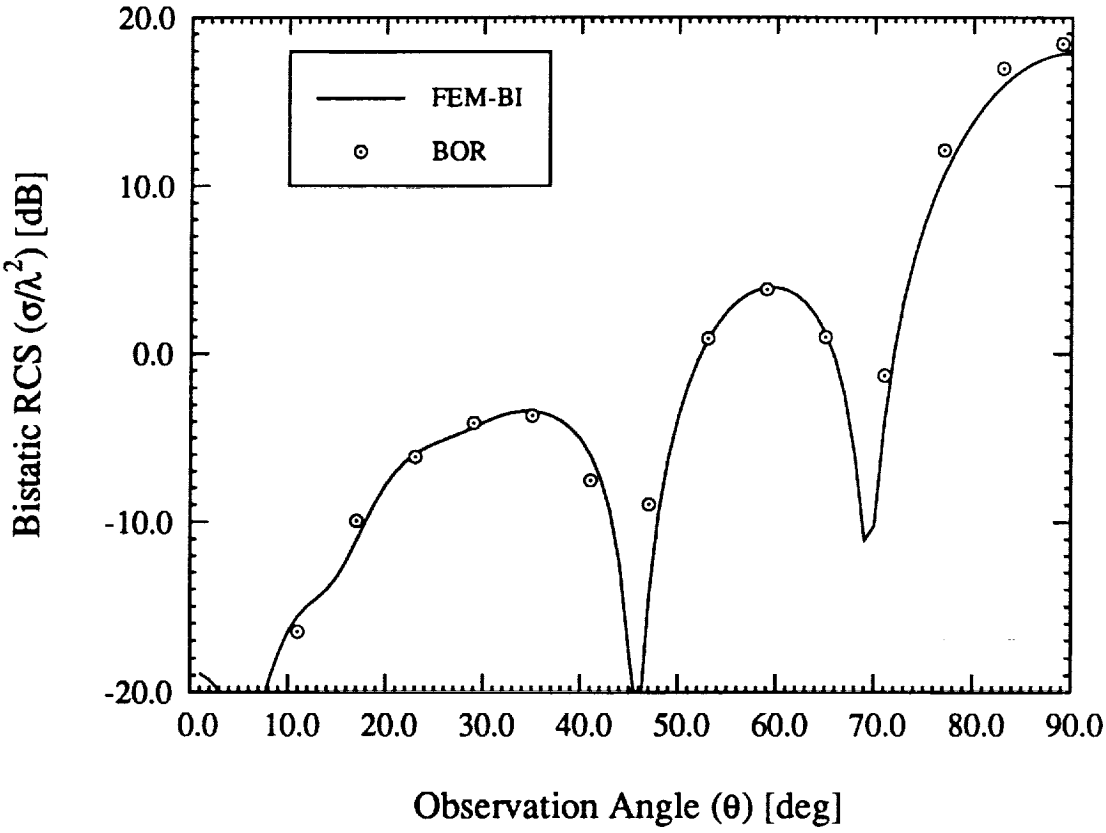


Figure 6: Comparison of the RCS computed via the FEM-BI method and a BOR code for a $3\lambda_0 \times 0.1\lambda_0$ air-filled wraparound cavity excited by a normally incident H-polarized ($\alpha = 90°$) plane wave.

this geometry as a function of frequency and curvature. Evidently, the resonance behavior of this patch is sensitive to curvature for both principal polarizations. The frequency response for E-polarization is more sensitive to curvature since the radiating surface field component is parallel to the long side of the patch and cavity. If the patch and cavity were oriented so that the long side is in the $\hat{\phi}$-direction, the response to H-polarization would exhibit greater sensitivity. Such an effect is important to low observable antenna designers since they want to operate the antenna in the region of lowest RCS. This low return region is a consequence of delicate cancellations due to the physical layout of the aperture. Such cancellations are not as complete for highly curved structures as they are for planar cavities.

Conformal antenna designers often use wraparound antennas to achieve omnidirectional coverage. Two different configurations are typically used: a wraparound cavity where the cavity is filled with a single continuous collar of dielectric and discrete cavities symmetrically placed around the circumference of the cylinder. These two configurations are shown in figure (9). Since near resonance, the radiation properties of these two types of antennas is identical, any RCS advantage which one might possess could govern the appropriate choice of arrays. Figure 10 compares the E-polarized monostatic scattering at 3 GHz in the $\theta = 90^{\circ}$ plane for a wraparound cavity and four discrete cavities; where the patches and cavities are identical to those used in the previous example. Not surprisingly, the wraparound structure has a higher return due to coupling within the substrate. However, since in this case the scattered field is due to the $z$ component of the surface field ($\phi$-directed magnetic currents), both cavities yield large scattered fields in the four directional lobes. Figure 11 is the corresponding comparison for H-polarization. In this case, the scattered field is attributed to the $\phi$ component of the surface fields (z-directed magnetic currents). Therefore, substrate modes diffract near the patch resulting in discrete lobes for the discrete array while creeping waves shed isotropically for the continuous wraparound cavity. Low observable designs will favor discrete cavity arrays over wraparound cavities since the scattering may be channeled in preferred directions and the overall scattering level is consistently lower. A final example is shown in figure 12 where we observe that other than the expected higher scattering from the wraparound cavity, the scattering behavior of the two arrays is very similar.

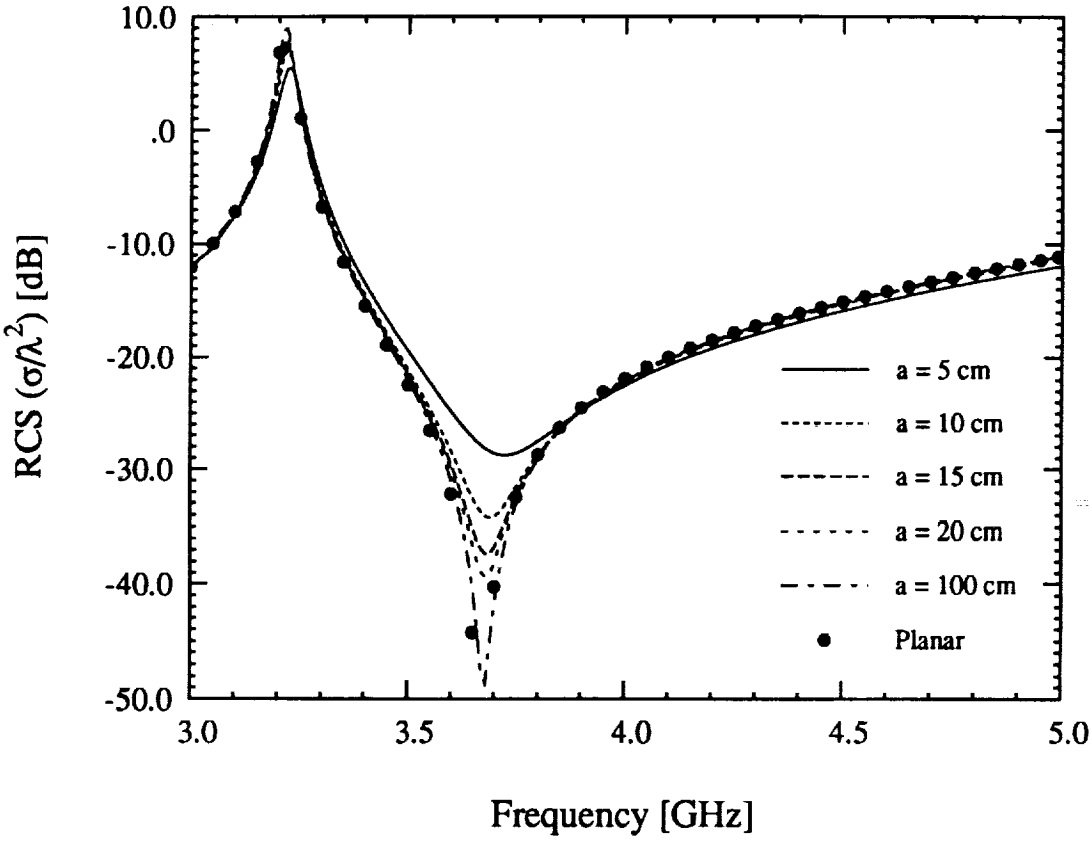


Figure 7: RCS frequency response for a 2 cm × 3 cm × patch residing in a 5 cm × 6 cm × 0.07874 cm cavity with $\epsilon_r = 2.17$ as a function of curvature for E-polarization ($\alpha = 0^o$).

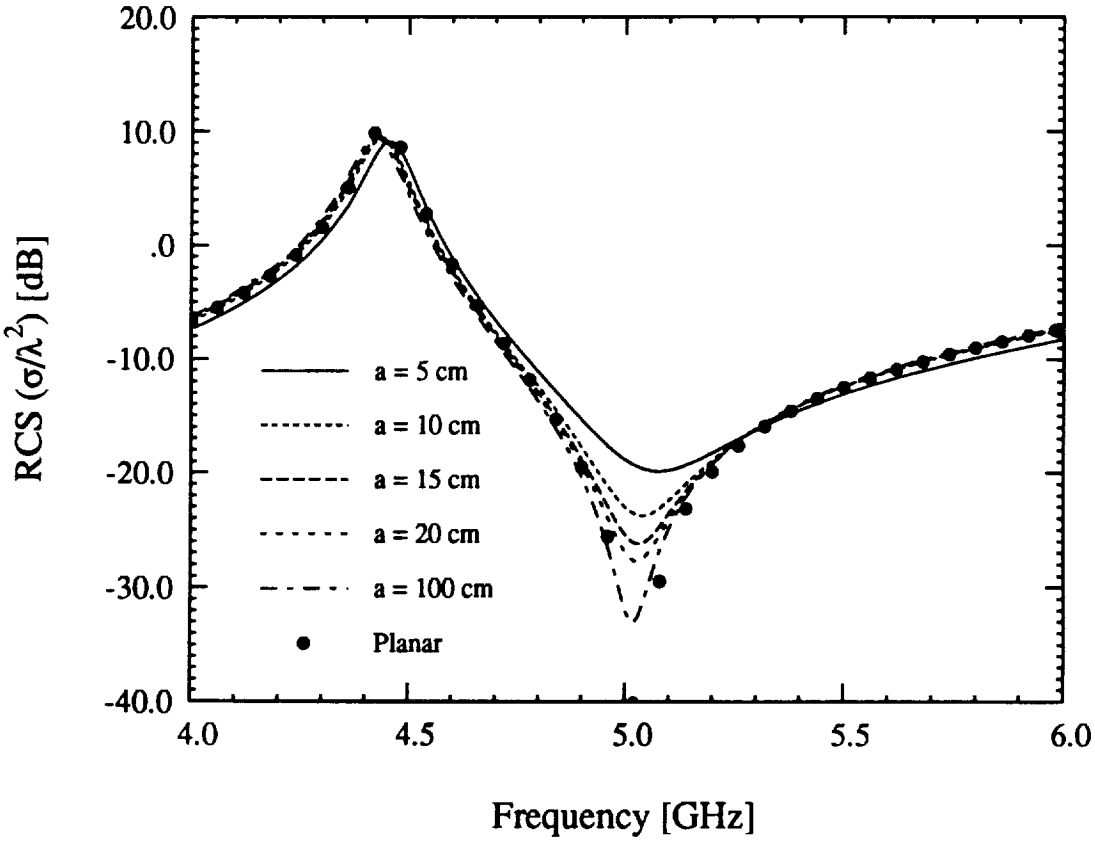


Figure 8: RCS frequency response for a 2 cm $\times$ 3 cm $\times$ patch residing in a 5 cm $\times$ 6 cm $\times$ 0.07874 cm cavity with $\epsilon_r = 2.17$ as a function of curvature for H-polarization ($\alpha = 90°$).

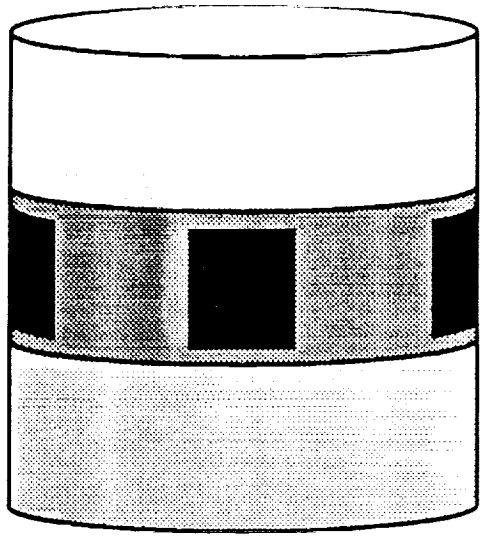

(a)

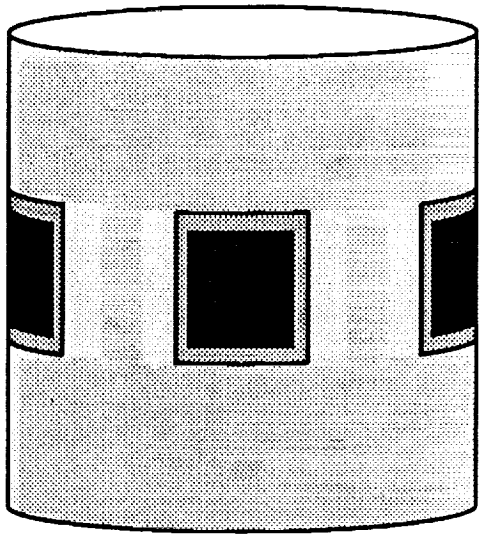

(b)

Figure 9: Illustration of two types of arrays: (a) wraparound array; (b) discrete cavity array

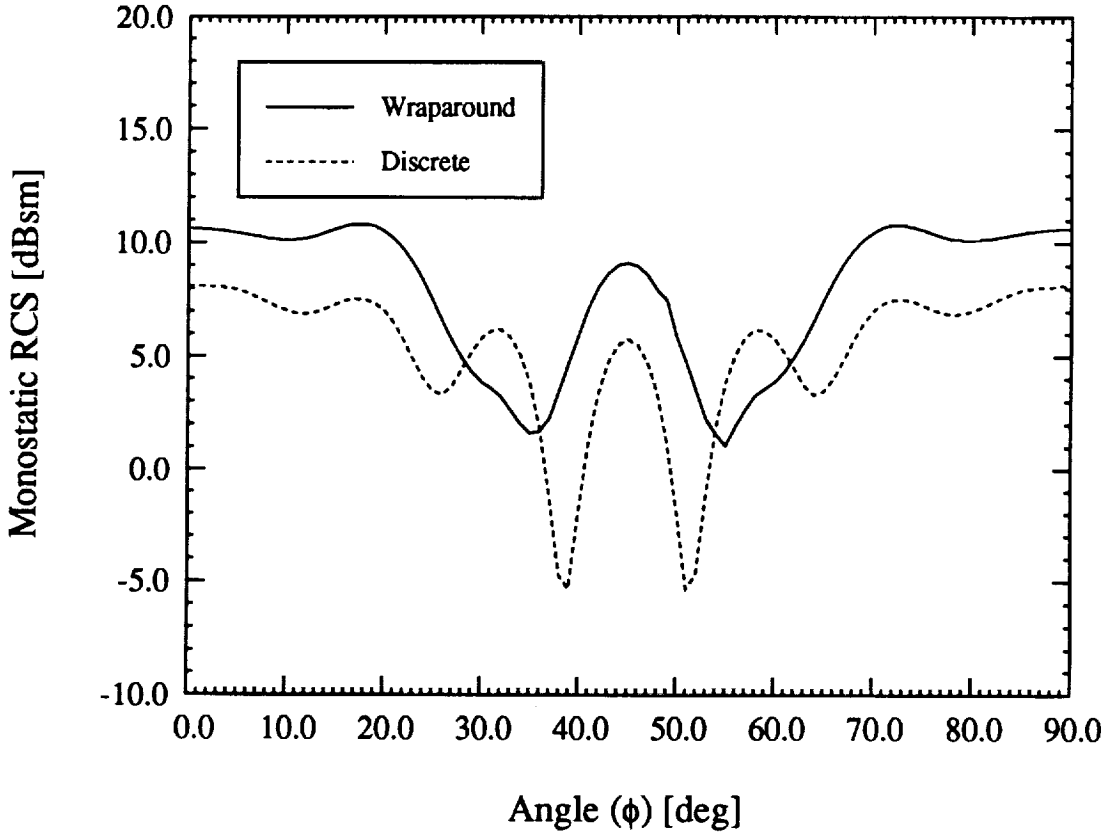


Figure 10: Comparison of E-polarized monostatic RCS at 3 GHz for a four patch array placed on a wraparound collar or in four discrete cavities. The patches and cavities are identical to the one used in figure 7. The observation plane is $\theta = 90^o$.

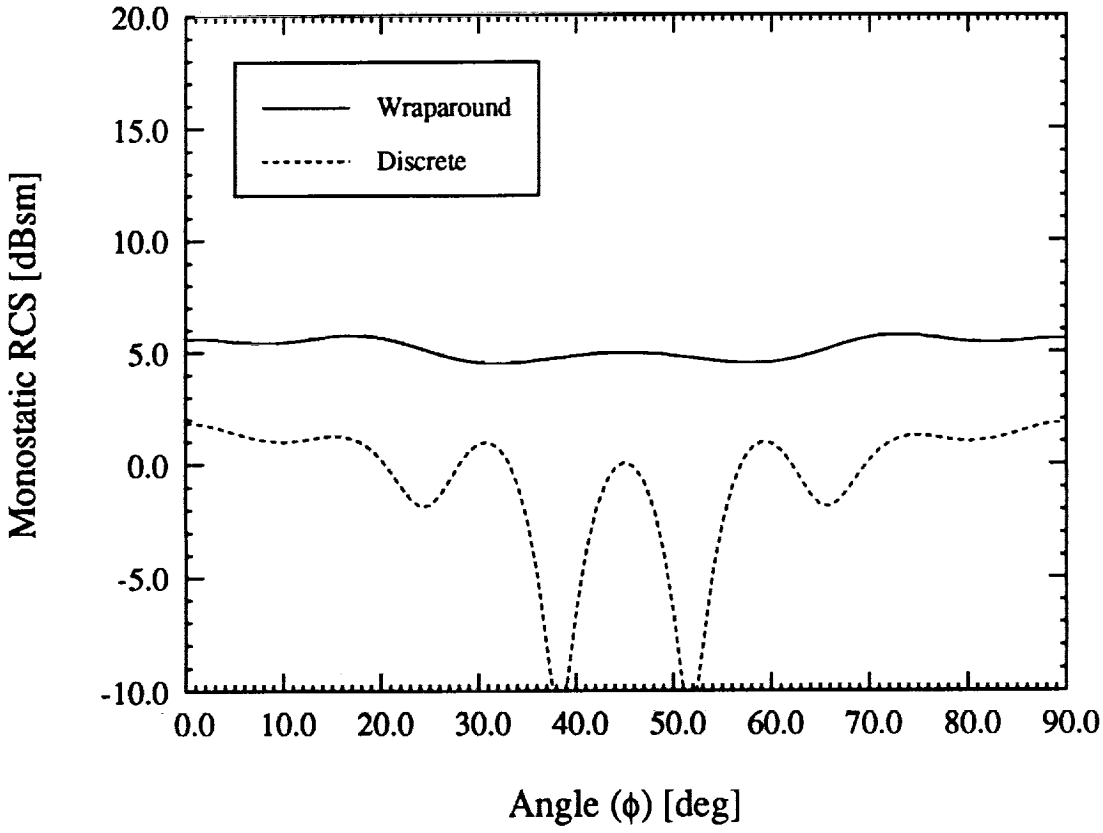


Figure 11: Comparison of H-polarized monostatic RCS at 3 GHz for a four patch array placed on a wraparound collar or in four discrete cavities. The patches and cavities are identical to the one used in figure 8. The observation plane is $\theta = 90°$.

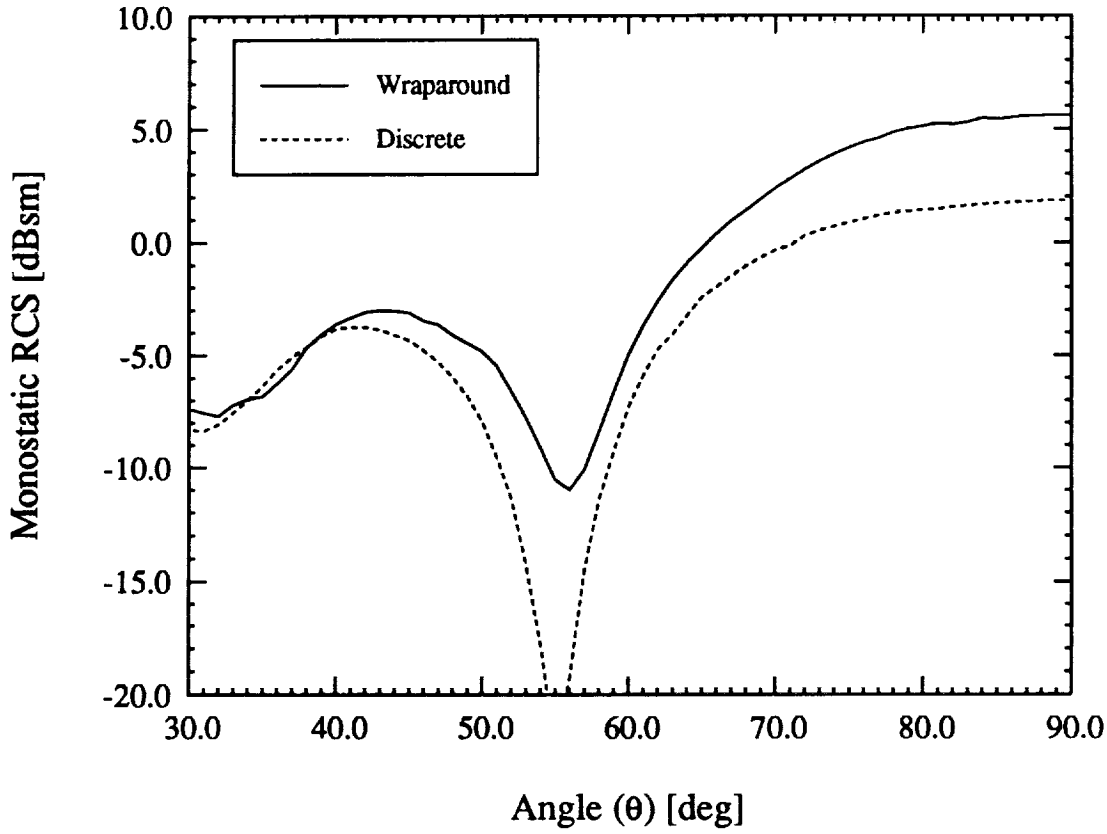


Figure 12: Comparison of H-polarized monostatic scattering at 3 GHz by a four patch array placed on a wraparound collar or in four discrete cavities. The patches and cavities are identical to the one used in figure 8. The observation plane is $\phi = 0°$.

# 6 Conclusions

In this paper, we have presented a Finite Element Method - Boundary Integral technique suitable for electromagnetic scattering calculations for cavities embedded within a circular, metallic cylinder. This formulation is analogous to the FEM-BI approach used by Jin and Volakis [1, 5, 6] and may accordingly be used for the analysis of scattering by a large array of cavity-backed patch antennas. These cavities need not be identical, periodically spaced or homogeneously filled and may in fact may possess lumped impedance loads or surface metallization layers. The FEM approach employs vector finite elements which properly represent the electromagnetic fields and possess high geometrical fidelity for cylindrical-rectangular cavities. Such elements were presented and are analogous to the bricks used for modeling rectangular cavities. In addition, we presented an efficient method for evaluating the on-surface and far-zone dyadic Green's functions. The presented formulation is amenable to solution using the BiCG-FFT method provided uniform zoning is used across the aperture and as a consequence, this implementation has low computational and memory demand. We have presented some validation of this work with appropriate limiting cases which provides further archival reference data. In addition, we showed how this formulation may be used to influence conformal antenna designs.

# References


[1] J-M Jin and J.L. Volakis, "A hybrid finite element method for scattering and radiation by microstrip patch antennas and arrays residing in a cavity," *IEEE Trans. Antennas and Propagat.*, Vol. 39, No. 11, pp. 1598-1604, Nov. 1991.

[2] J.L. Volakis, A. Chatterjee and J. Gong, "A class of hybrid finite element methods for electromagnetics: A review," to appear in *J. Electromagnetic Waves Appl.*, 1994.

[3] Z.J. Cendes, "Vector finite elements for electromagnetic field computation," *IEEE Trans. Magnetics*, Vol. 27, No. 5, pp. 3958-3966, Sept. 1991.

[4] A. Bossavit, "A rationale for edge-elements in 3D fields computations," *IEEE Trans. Magnetics* Vol. 24, No. 1, pp. 74-79, Jan 1988.

[5] J-M Jin and J.L. Volakis, "A finite element-boundary integral formulation for scattering by three-dimensional cavity-backed apertures," *IEEE Trans. Antennas and Propagat.*, Vol. 39, No. 1, pp. 97-104, Jan. 1991.

[6] J-M Jin and J.L. Volakis, "Electromagnetic scattering by and transmission through a three-dimensional slot in a thick conducting plane," *IEEE Trans. Antennas and Propagat.*, Vol. 39, No. 4, pp. 543-550, Apr. 1991.

[7] A. Chatterjee, J-M. Jin, and J.L. Volakis, "Computation of cavity resonances using edge-based finite elements," *IEEE Trans. Microwave Theory Tech.*, Vol. 40, No. 11, pp. 2106-2108, Nov. 1992.

[8] C-T Tai, *Dyadic Green's Functions in Electromagnetic Theory* . International Textbook Co., Scranton, 1971.

[9] P.H. Pathak and N.N. Wang, "An analysis of the mutual coupling between antennas on a smooth convex surface," *Ohio State Univ. Electro-Science Lab.*, Report 784583-7, Oct. 1978.

[10] J. Boersma and S.W. Lee, "Surface field due to a magnetic dipole on a cylinder: Asymptotic expansions of exact solution," *Univ. Illinois Electromagnetics Lab.*, Report 78-17, 1978.

[11] T.S. Bird, "Comparison of asymptotic solutions for the surface field excited by a magnetic dipole on a cylinder," *IEEE Trans. Antennas and Propagat.*, Vol. 32, No. 11, pp. 1237-1244, Nov. 1984.

[12] T.S. Bird, "Accurate asymptotic solution for the surface field due to apertures in a conducting cylinder," *IEEE Trans. Antennas and Propagat.*, Vol. 33, No. 10, pp. 1108-1117, Oct. 1985.

[13] N. A. Logan, "General research in diffraction theory," *Lockheed Aircraft Corp., Missiles and Space Div.*, vol. 1 and 2, Report LMSD-288088, Dec. 1959.

[14] O. Einarsson, R.E. Kleinman, P. Laurin, and P.L.E. Uslenghi, "Studies in radar cross sections L - Diffraction and scattering by regular bodies IV: The circular cylinder," *University of Michigan Technical Report* No. 7133-3-T, 1966.

[15] A.S. Goriainov, "An asymptotic solution of the problem of diffraction of a plane electromagnetic wave by a conducting cylinder," *Radio Engr. and Electr. Phys.*, Vol. 3, pp. 23-39 , 1958. (English translation of *Radiotekhnica i Elektronica*, Vol. 3)

[16] T.K. Sarkar, "On the application of the generalized biconjugate gradient method," *J. Electromagnetic Waves Appl.*, Vol. 1, No. 3, pp. 223-242, 1987.

[17] C.F. Smith, A.F. Peterson and R. Mittra, "The biconjugate gradient method for electromagnetic scattering," *IEEE Trans. Antennas and Propagat.*, Vol. 38, No. 6, pp. 938-940, June 1990.

# Appendices

## A FEM Matrix Entries

The matrix entries for the FEM portion of the system (5) are given in this appendix assuming that the cylindrical shell elements (4) are used in (6). These integrals are given by

$$
\begin{aligned}
I_{\rho\rho}^{(1)} &= \frac{\tilde{s}_s\tilde{s}_t}{(\alpha h)^2}\Big[\rho_b^2 h \ln\left(\frac{\rho_b}{\rho_a}\right)\int_{\phi_l}^{\phi_r}(\phi-\tilde{\phi}_s)(\phi-\tilde{\phi}_t)d\phi + \\
&\qquad \frac{\alpha}{2}\left(\frac{\rho_b^2}{\rho_a^2}-1\right)\int_{z_b}^{z_t}(z-\tilde{z}_s)(z-\tilde{z}_t)dz\Big] \\
I_{\rho\phi}^{(1)} &= -\frac{\tilde{s}_s\tilde{s}_t}{th^2}\left[2\rho_b\ln\left(\frac{\rho_b}{\rho_a}\right)+\tilde{\rho}_t\left(1-\frac{\rho_b}{\rho_a}\right)\right]\int_{z_b}^{z_t}(z-\tilde{z}_s)(z-\tilde{z}_t)dz \\
I_{\rho z}^{(1)} &= -\frac{\tilde{s}_s\tilde{s}_t\rho_b}{\alpha^2}\int_{\phi_l}^{\phi_r}(\phi-\tilde{\phi}_s)(\phi-\tilde{\phi}_t)d\phi \\
I_{\phi\phi}^{(1)} &= \frac{\tilde{s}_s\tilde{s}_t\alpha}{(th)^2}\Big[h\left(\frac{1}{4}\left(\rho_b^4-\rho_a^4\right)+\frac{1}{3}\left(\tilde{\rho}_s+\tilde{\rho}_t\right)\left(\rho_a^3-\rho_b^3\right)+\frac{1}{2}\tilde{\rho}_s\tilde{\rho}_t\left(\rho_b^2-\rho_a^2\right)\right)+ \\
&\qquad \left(2\left(\rho_b^2-\rho_a^2\right)-2t\left(\tilde{\rho}_s+\tilde{\rho}_t\right)+\tilde{\rho}_s\tilde{\rho}_t\ln\left(\frac{\rho_b}{\rho_a}\right)\right)\int_{z_b}^{z_t}(z-\tilde{z}_s)(z-\tilde{z}_t)dz\Big] \\
I_{\phi z}^{(1)} &= -\frac{\tilde{s}_s\tilde{s}_t}{t^2}\int_{\rho_a}^{\rho_b}(\rho-\tilde{\rho}_s)(\rho-\tilde{\rho}_t)d\rho \\
I_{zz}^{(1)} &= \frac{\tilde{s}_s\tilde{s}_t h}{(t\alpha)^2}\Big[\alpha\left(\frac{1}{2}\left(\rho_b^2-\rho_a^2\right)-t\left(\tilde{\rho}_s+\tilde{\rho}_t\right)+\tilde{\rho}_s\tilde{\rho}_t\ln\left(\frac{\rho_b}{\rho_a}\right)\right)+ \\
&\qquad \frac{1}{2}\left(\rho_b^2-\rho_a^2\right)\int_{\phi_l}^{\phi_r}(\phi-\tilde{\phi}_s)(\phi-\tilde{\phi}_t)d\phi\Big] \\
I_{\rho\rho}^{(2)} &= \frac{\tilde{s}_s\tilde{s}_t\rho_b^2}{(\alpha h)^2}\ln\left(\frac{\rho_b}{\rho_a}\right)\int_{\phi_l}^{\phi_r}(\phi-\tilde{\phi}_s)(\phi-\tilde{\phi}_t)d\phi\int_{z_b}^{z_t}(z-\tilde{z}_s)(z-\tilde{z}_t)dz \\
I_{\phi\phi}^{(2)} &= \frac{\tilde{s}_s\tilde{s}_t\alpha}{(th)^2}\left[\frac{1}{4}\left(\rho_b^4-\rho_a^4\right)+\frac{1}{3}\left(\tilde{\rho}_s+\tilde{\rho}_t\right)\left(\rho_a^3-\rho_b^3\right)+\frac{1}{2}\tilde{\rho}_s\tilde{\rho}_t\left(\rho_b^2-\rho_a^2\right)\right]\times \\
&\qquad \int_{z_b}^{z_t}(z-\tilde{z}_s)(z-\tilde{z}_t)dz \\
I_{zz}^{(2)} &= \frac{\tilde{s}_s\tilde{s}_t h}{(t\alpha)^2}\left[\frac{1}{4}\left(\rho_b^4-\rho_a^4\right)+\frac{1}{3}\left(\tilde{\rho}_s+\tilde{\rho}_t\right)\left(\rho_a^3-\rho_b^3\right)+\frac{1}{2}\tilde{\rho}_s\tilde{\rho}_t\left(\rho_b^2-\rho_a^2\right)\right]\times
\end{aligned}
$$

$$\int_{\phi_l}^{\phi_r} (\phi - \tilde{\phi}_s)(\phi - \tilde{\phi}_t) d\phi \qquad \text{(A-1)}$$

Each of the above unevaluated integrals is of the form

$$\int_L^U \left(\xi - \tilde{\xi}_s\right)\left(\xi - \tilde{\xi}_t\right) d\xi = \frac{1}{2}\left(L^2 - U^2\right)\left(\tilde{\xi}_s + \tilde{\xi}_t\right) + \frac{1}{3}\left(U^3 - L^3\right) + \tilde{\xi}_s\tilde{\xi}_t\,(U - L) \qquad \text{(A-2)}$$

The integrals $I_{st}^{(1),(2)}$ are used in the assembly of the FEM portion ($[\mathcal{A}]$) of the system.

# B Fock Functions

The asymptotic form of the dyadic Green's function with observation both on the surface of the cylinder and in the far field involves Fock functions. These have been extensively studied and tabulated by Logan [13]. The numerical evaluation of these functions are performed either for small arguments or large arguments.

The on-surface Fock functions used in this paper are

$$\begin{aligned} v(\xi) &= \frac{1}{2} e^{j\pi/4} \sqrt{\frac{\xi}{\pi}} \int_{\infty e^{-j2\pi/3}}^{\infty} \frac{w_2(\tau)}{w_2'(\tau)} e^{-j\xi\tau} d\tau \\ u(\xi) &= e^{j3\pi/4} \frac{\xi^{\frac{3}{2}}}{\sqrt{\pi}} \int_{\infty e^{-j2\pi/3}}^{\infty} \frac{w_2'(\tau)}{w_2(\tau)} e^{-j\xi\tau} d\tau \end{aligned} \qquad \text{(B-1)}$$

where $w_2(\tau)$ and its derivative $w_2'(\tau)$ denote Airy functions of the Second Kind. For small arguments ($\xi < 0.6$), the asymptotic expansion of (B-1) is given by

$$\begin{aligned} v(\xi) &\sim 1.0 - \frac{\sqrt{\pi}}{4}\xi^{\frac{3}{2}} + j\frac{7}{60}\xi^3 + \frac{7}{512}\sqrt{\pi} e^{-j\frac{\pi}{4}} \xi^{\frac{9}{2}} + \ldots \\ u(\xi) &\sim 1.0 - \frac{\sqrt{\pi}}{2} e^{-j\frac{\pi}{4}} \xi^{\frac{3}{2}} + j\frac{5}{12}\xi^3 + \frac{5}{64}\sqrt{\pi} e^{-j\frac{\pi}{4}} \xi^{\frac{9}{2}} + \ldots \end{aligned} \qquad \text{(B-2)}$$

while a rapidly converging residue series is used for $\xi > 0.6$

$$v(\xi) \sim = e^{-j\frac{\pi}{4}} \sqrt{\pi\xi} \sum_{n=1}^{10} \left(\tau_n'\right)^{-1} e^{-j\xi\tau_n'}$$

$$u(\xi) \sim = 2e^{j\frac{\pi}{4}}\sqrt{\pi}\xi^{\frac{3}{2}}\sum_{n=1}^{10}(\tau_n)^{-1}\, e^{-j\xi\tau_n} \qquad \text{(B-3)}$$

where $\tau_n$ and $\tau_n^{'}$ are zeros of $w_2(\tau)$ and $w_2'(\tau)$, respectively. Those zeros are given in the following table

Table B-1
Zeros of the $w_2(\tau)$ and $w_2'(\tau)$
$\tau_n = |\tau_n|e^{-j\frac{\pi}{3}}$ and $\tau_n^{'} = |\tau_n^{'}|e^{-j\frac{\pi}{3}}$

| n | $\lvert\tau_n\rvert$ | $\lvert\tau_n^{'}\rvert$ |
|---|---|---|
| 1 | 2.33811 | 1.011879 |
| 2 | 4.08795 | 3.24819 |
| 3 | 5.52056 | 4.82010 |
| 4 | 6.78661 | 6.16331 |
| 5 | 7.94413 | 7.37218 |
| 6 | 9.02265 | 8.48849 |
| 7 | 10.0402 | 9.53545 |
| 8 | 11.0085 | 10.5277 |
| 9 | 11.9300 | 11.4751 |
| 10 | 12.8288 | 12.3848 |

The far-zone Fock functions are given by

$$\begin{aligned} g^{(l)}(\xi) &= \frac{j^l}{\sqrt{\pi}}\int_\Gamma \frac{e^{j\xi\tau}}{w_1'(\tau)}d\tau \\ f^{(l)}(\xi) &= \frac{j^l}{\sqrt{\pi}}\int_\Gamma \frac{e^{j\xi\tau}}{w_1(\tau)}d\tau \\ G^{(l)}(\xi) &= g^{(l)}(\xi)e^{j\frac{\xi^3}{3}} \\ F^{(l)}(\xi) &= f^{(l)}(\xi)e^{j\frac{\xi^3}{3}} \end{aligned} \qquad \text{(B-4)}$$

where $w_1(\tau)$ and its derivative $w_1'(\tau)$ denote Airy functions of the First Kind and the integration contour is given by Logan [13]. These functions, $g^{(0)}(\xi)$, $g^{(1)}(\xi)$ and $f^{(0)}(\xi)$, may be calculated using

$$
\begin{aligned}
g^{(0)}(\xi) &= 2.0e^{-j\frac{\xi^3}{3}} \quad \xi < -1.3 \\
&= 1.39937 + \sum_{m=1}^{6} \frac{c(m)}{m!} (\kappa\xi)^m \quad -1.3 \leq \xi \leq 0.5 \\
&= \sum_{m=1}^{10} \frac{e^{\left[\kappa\alpha'(m)\xi\right]}}{\alpha'(m)Ai(m)} \quad 0.5 < \xi \leq 4.0 \\
&= 1.8325e^{\left[-(0.8823-j0.5094)\xi - j\frac{\xi^3}{3}\right]} \quad \xi > 4.0
\end{aligned} \tag{B-5}
$$

$$
\begin{aligned}
g^{(1)}(\xi) &= -j2.0\left(\xi^2 + j\frac{0.25}{\xi} - \frac{0.25}{\xi^4}\right) e^{-j\frac{\xi^3}{3}} \quad \xi < -2.8 \\
&= \sum_{m=1}^{6} \frac{c(m)\kappa^m}{m!} (\xi)^{m-1} \quad -2.8 \leq \xi \leq 0.5 \\
&= \kappa \sum_{m=1}^{10} \frac{e^{[\kappa\alpha(m)\xi]}}{Ai(m)} \quad 0.5 < \xi \leq 4.0 \\
&= -1.8325\left(0.8823 - j0.5094 + j\xi^2\right) e^{\left[-(0.8823-j0.5094)\xi - j\frac{\xi^3}{3}\right]} \quad \xi > 4.0
\end{aligned} \tag{B-6}
$$

$$
\begin{aligned}
f^{(0)}(\xi) &= j2\xi\left(1 - \frac{0.25}{\xi^3} + \frac{0.5}{\xi^6}\right) e^{-j\frac{\xi^3}{3}} \quad \xi < -1.1 \\
&= 0.77582 + e^{-j\pi/3} \sum_{m=1}^{6} \frac{c(m)}{m!} (\kappa\xi)^m \quad -1.1 \leq \xi \leq 0.5 \\
&= e^{-j\pi/3} \sum_{m=1}^{10} \frac{e^{[\kappa\alpha(m)\xi]}}{Ai'(m)} \quad 0.5 < \xi \leq 4.0 \\
&= 0.0 \quad \xi > 4.0
\end{aligned} \tag{B-7}
$$

with constant $\kappa = e^{-j5\pi/6}$ and the coefficients for (B–5) and (B–6) given in the following table

| Table B-2<br>Constants for (B–5) and (B–6) | | | |
|---|---|---|---|
| m | c(m) | $\alpha'(m)$ | $Ai$(m) |
| 1 | 0.7473831 | 1.01879297 | 0.5356566 |
| 2 | -0.6862081 | 3.2481975 | -0.41901548 |
| 3 | -2.9495325 | 4.82009921 | 0.38040647 |
| 4 | -3.4827075 | 6.16330736 | -0.35790794 |
| 5 | 8.9378967 | 7.37217726 | 0.34230124 |
| 6 | 56.1946214 | 8.48848673 | -0.33047623 |
| 7 | | 9.53544905 | 0.32102229 |
| 8 | | 10.52766040 | -0.31318539 |
| 9 | | 11.47505663 | 0.30651729 |
| 10 | | 12.38478837 | -0.30073083 |

The corresponding constants for (B–7) are given as

| Table B-3<br>Constants for (B–7) | | | |
|---|---|---|---|
| m | c(m) | $\alpha(m)$ | $Ai'$(m) |
| 1 | 1.146730417 | 2.33810741 | 0.70121082 |
| 2 | 0.86284558 | 4.08794944 | -0.80311137 |
| 3 | -2.0192636 | 5.52055983 | 0.86520403 |
| 4 | -9.977776 | 6.78670809 | -0.91085074 |
| 5 | -14.59904 | 7.94413359 | 0.94733571 |
| 6 | 49.0751 | 9.02265085 | -0.97792281 |
| 7 | | 10.04017434 | 1.00437012 |
| 8 | | 11.00852430 | -1.02773869 |
| 9 | | 11.93601556 | 1.04872065 |
| 10 | | 12.82877675 | -1.06779386 |